ADVANCED ENERGY & SUSTAINABILITY RESEARCH
www.advenergysustres.com

Multifunctional Structural Electrolyte with Glass Fiber-Reinforced Polyvinyl Alcohol/Epoxy Matrix with Optimized Lithium Salt and Nanofiller

Maryam Niazi, Diana Paiva, Federico Danzi, Tânia Lopes, Adélio Mendes, and Pedro P. Camanho*

A novel multifunctional structural electrolyte is developed using plain–weave glass fiber reinforced with a composite polymer matrix for load-bearing energy-storage applications such as structural batteries. The composite matrix comprises polyvinyl alcohol (PVA) blended with epoxy, LiTFSI salt, and Al_2O_3 at optimized ratios. A set of techniques is used to evaluate and optimize the thermo-electro-mechanical properties of the matrix, including dynamic mechanical analysis (DMA), potentiostatic electrochemical impedance spectroscopy (PEIS), thermogravimetric analysis, differential scanning calorimetry, and X-ray diffraction. The optimization reveals a clear trade-off: increasing salt content enhances ionic conductivity but compromises mechanical properties, while the addition of nanofiller improves stiffness but reduces ionic conductivity. Based on multifunctionally balancing, a formulation of $PVA_{0.34}/epoxy_{0.14}/LiTFSI_{0.32}/(Al_2O_3)_{0.2}$ is obtained. The structural electrolyte, composed of glass fiber impregnated with the optimized matrix, is characterized using PEIS, DMA, tensile testing, and charge–discharge tests within lithium iron phosphate (LFP)/lithium metal and LFP/graphite cells. The electrolyte exhibits a storage modulus of 3 GPa, an ionic conductivity of 1.74×10^{-4} S cm^{-1}, a bulk stiffness of 1.82 GPa, and a tensile strength of 56.9 MPa. Full-cell testing demonstrates long cycle life and stable cyclability for ≈240 cycles, maintaining a high Coulombic efficiency of around 95% throughout cycling.

1. Introduction

Structural batteries are advanced systems that integrate load-bearing and energy-storage functions into a single structure, reducing weight and improving efficiency in applications such as electric vehicles and aerospace.[1–5] However, one of their main challenges is the development of a structural electrolyte that offers both high ionic conductivity and sufficient mechanical integrity.[6–9] Composite polymer electrolytes (CPEs) are promising candidates for structural battery applications due to their mechanical strength, flexibility, interfacial compatibility, ease of processing, and enhanced safety.[10–13] However, because CPEs are typically based on thermoplastic polymer hosts, they tend to lose mechanical strength at elevated temperatures caused by internal electrochemical reactions or external environmental thermal exposure (e.g., sunlight). This limitation is addressed by incorporating heat-resistant thermoset polymers (e.g., epoxy) and carefully optimizing lithium salt and nanofiller concentrations to produce a composite electrolyte matrix with superior thermo-electro-mechanical performance. The optimized matrix is subsequently used to impregnate a glass fiber fabric, thereby further improving thermal stability, load-bearing capability, and ionic conductivity. Additionally, a modified solution-casting approach (combining conventional solution casting with in situ drying under pressure and heat) is employed to overcome the common limitation of poor

M. Niazi, P. P. Camanho
INEGI
Faculdade de Engenharia
Universidade do Porto
Rua Dr. Roberto Frias 400, Porto 4200-465, Portugal
E-mail: up202103277@edu.fe.up.pt

The ORCID identification number(s) for the author(s) of this article can be found under https://doi.org/10.1002/aesr.202500222.

© 2025 The Author(s). Advanced Energy and Sustainability Research published by Wiley-VCH GmbH. This is an open access article under the terms of the Creative Commons Attribution License, which permits use, distribution and reproduction in any medium, provided the original work is properly cited.

DOI: 10.1002/aesr.202500222

D. Paiva, T. Lopes, A. Mendes
LEPABE
Faculdade de Engenharia
Universidade do Porto
Rua Dr. Roberto Frias s/n, Porto 4200-465, Portugal

D. Paiva, T. Lopes, A. Mendes
ALiCE
Faculdade de Engenharia
Universidade do Porto
Rua Dr. Roberto Frias s/n, Porto 4200-465, Portugal

F. Danzi
INEGI
Instituto de Ciência e Inovação em Engenharia Mecânica e Engenharia Industrial
Universidade do Porto
Rua Dr. Roberto Frias 400, Porto 4200-465, Portugal

26999412, 0, Downloaded from https://advanced.onlinelibrary.wiley.com/doi/10.1002/aesr.202500222 by Universidade do Porto, Wiley Online Library on [21/10/2025]. See the Terms and Conditions (https://onlinelibrary.wiley.com/terms-and-conditions) on Wiley Online Library for rules of use; OA articles are governed by the applicable Creative Commons License

interfacial contact encountered in conventional solution casting.[2,14] Various thermoplastic polymers (e.g., PVC, PVA, PEO, PAN, PVdF, PMMA, and chitosan) have been used as electrolyte hosts.[15–21] Among these, PVA stands out for its high dielectric constant, excellent mechanical properties, biodegradability, and cost-effectiveness.[22] Thermoplastic hosts are favored in electrolytes for their high ionic conductivity,[23] but they tend to soften when heated. Although this softening improves ionic conductivity at elevated temperatures, it significantly compromises mechanical performance. In contrast, thermoset polymers such as epoxy exhibit outstanding thermomechanical stability. However, extensive cross-linking in thermosets restricts the mobility of polymer chains and ions, resulting in very low ionic conductivity (typically below 10^{-12} S cm^{-1} at room temperature).[24] Therefore, combining thermoset and thermoplastic polymers offers a promising strategy for creating a composite electrolyte matrix that leverages the strengths of both.[25,26] Salts and nanofillers strongly influence the electrochemical and mechanical properties of the composite polymer matrix. Initially, increasing lithium salt concentration enhances ionic conductivity by plasticizing the polymer and increasing ion mobility. However, beyond an optimal concentration, further salt addition leads to diminishing returns or reduced conductivity due to ion-pairing, polymer-salt complexation, and phase separation.[27–31] Salt content can also plasticize the polymer matrix and reduce its stiffness and tensile strength.[32] Inorganic nanofillers such as Al_2O_3 and $Li_7La_3Zr_2O_{12}$ are commonly incorporated into polymer electrolytes to enhance their mechanical strength. However, their effects on polymer crystallinity and ionic conductivity can vary depending on several factors. Some studies have shown that when well dispersed, these rigid particles can disrupt polymer chain packing, increase the amorphous fraction, and lower the glass transition temperature, thereby enhancing segmental mobility and facilitating ion transport.[33,34] Conversely, other studies have demonstrated that nanofillers can also act as nucleating agents, promoting crystallization rather than suppressing it, which may slightly reduce ionic conductivity.[35] Optimizing the concentrations of both salt and filler is thus critical to balance mechanical integrity with electrochemical performance in structural battery applications.

Several fabrication techniques exist for polymer electrolytes, including solution casting,[36] solvent-free methods,[37,38] phase inversion,[39] electrospinning,[40] in situ polymerization,[41] and layer-by-layer deposition.[42] Solution casting is widely favored for its simplicity, uniform dispersion, and scalability, but it often suffers from poor interfacial contact with electrodes, which can limit energy density.[2] In contrast, techniques like in situ polymerization can enhance the polymer–electrode interface by polymerizing the polymer electrolyte directly on the electrodes or within the cell. However, these methods may introduce issues such as voids, dead volume, and added weight during manufacturing.[43] Recent studies have shown that applying additional steps, such as wetting the film and in situ drying it with heat and pressure, can improve interfacial contact.[14] A recent study[14] compared different solvents (NMP, water, DMSO) for dissolving PVA and blending with epoxy. DMSO yielded the highest ionic conductivity in the thermoplastic/epoxy film without severely reacting with or dissolving the epoxy. In contrast, NMP resulted in lower conductivity. In contrast, NMP produced lower conductivity. Although water evaporated readily, it was avoided in this work because even minor traces of moisture content (ppm-level) can adversely affect battery recyclability.[44] Accurate quantification of any residual solvents or absorbed moisture in the polymer films is essential, since even trace amounts can alter the glass transition and plasticization of the polymer matrix, thereby impacting ionic conductivity and mechanical properties.[44,45] In this study, a composite polymer electrolyte—comprising PVA blended with epoxy resin, LiTFSI salt, and Al_2O_3 nanofiller at optimized ratios—was first developed and then used as the polymer matrix for reinforcing a glass fiber separator to form a structural electrolyte. The paper is structured as follows: Section 2 presents the results and discussion, Section 3 summarizes the conclusions, and Section 4 details the materials and methods. The first part of Section 2 focuses on the optimization of the salt and nanofiller content to obtain the composite matrix. This optimization was guided by results from potentiostatic electrochemical impedance spectroscopy (PEIS), dynamic mechanical analysis (DMA), thermogravimetric analysis (TGA), differential scanning calorimetry (DSC), and X-ray diffraction (XRD). The second part of Section 2 discusses the characterization of the structural electrolyte, which consists of glass fiber reinforced with the optimized polymer matrix. The thermo-electro-mechanical properties of the structural electrolyte are evaluated using PEIS, DMA, TGA, and tensile testing to determine ionic conductivity, thermomechanical stability, solvent content, stiffness, strength, and failure strain. Furthermore, the structural electrolyte was tested electrochemically in both half-cell configuration—using commercial $LiFePO_4$ (LFP) foil as cathode and lithium metal as anode—and full-cell configuration with custom-made LFP-coated on aluminum foil and custom-made graphite-coated on copper foil.

2. Results and Discussion

2.1. Composite Polymer Electrolyte: Optimization of Salt and Nanofiller

2.1.1. Thermomechanical, Thermogravimetric, and Structural Results

The thermomechanical and thermogravimetric results of polymeric films containing different amounts of LiTFSI and Al_2O_3 are shown in **Figure 1**. Figure 1a shows the results for PVA/epoxy films with varying concentrations of LiTFSI. As the LiTFSI salt content increases, the storage modulus decreases due to the plasticizing effect of LiTFSI, which is consistent with the literature.[32] In addition, thin films with lower LiTFSI concentrations exhibit a pronounced reduction in storage modulus as the temperature increases, indicating higher sensitivity to thermal softening. In contrast, films with higher LiTFSI concentrations also show modulus decrease at elevated temperatures; however, the reduction is notably smaller. This suggests that higher LiTFSI content contributes to improved thermomechanical stability of the polymer network, potentially through enhanced ionic cross-linking or increased salt–polymer interactions that reinforce the structural integrity of the material at high temperatures. For instance, in thin films containing 10 wt% LiTFSI, the storage modulus dropped from 85 to 32 MPa upon

© 2025 The Author(s). Advanced Energy and Sustainability Research published by Wiley-VCH GmbH

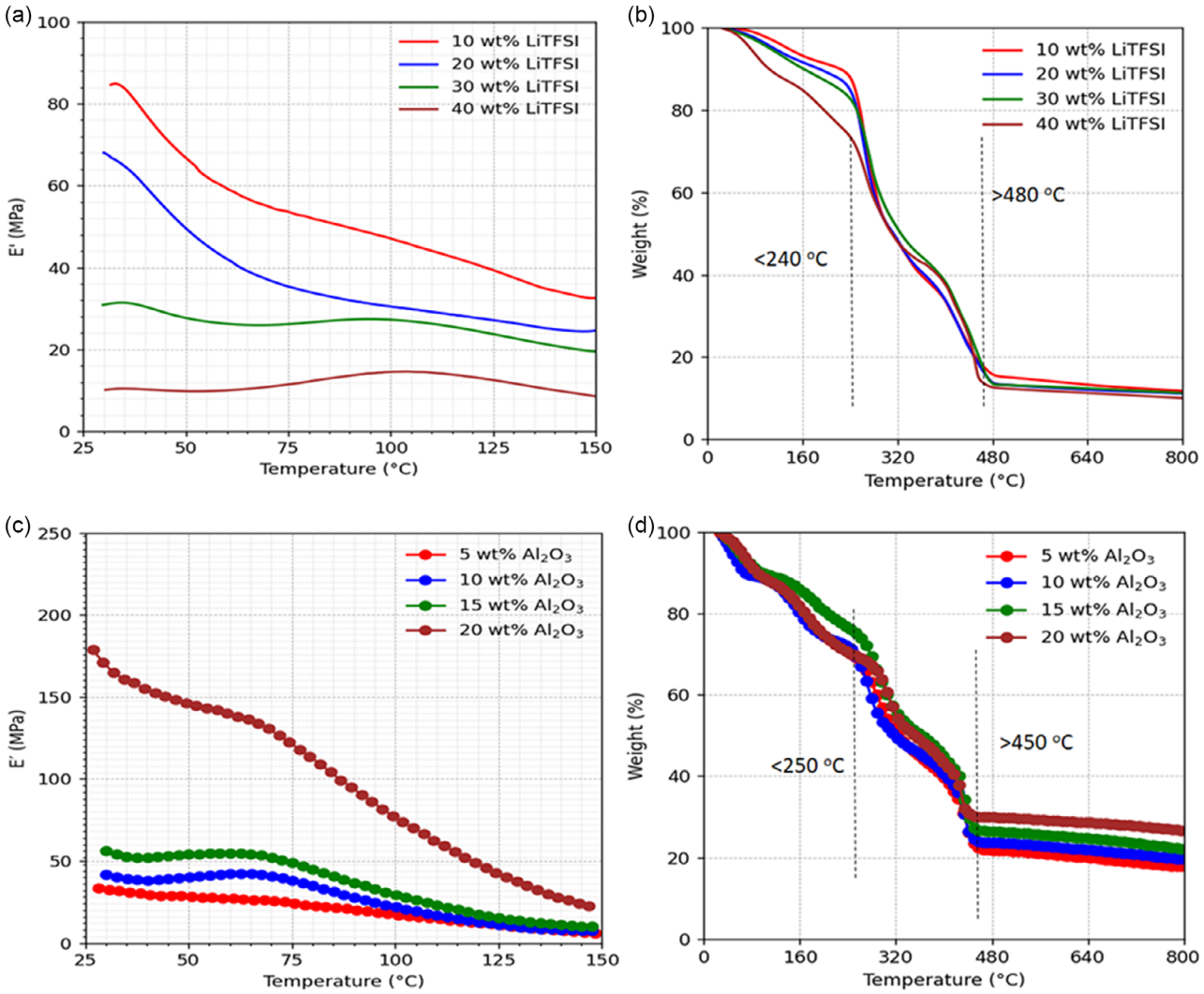


Figure 1. Thermomechanical and thermogravimetric results: a) Storage modulus (E') and b) TGA of PVA/epoxy films with different concentrations of LiTFSI; c) Storage modulus (E') and d) TGA of PVA/epoxy/LiTFSI films with different concentrations of Al_2O_3.

heating to 150 °C, a 62% decrease. In contrast, films with 40 wt% LiTFSI showed a less pronounced decline, from 10 to 8.3 MPa, representing only a 17% decrease. Inside a polymer film, increasing temperature enhances the mobility of polymer chains, leading to a reduction in storage modulus. Interestingly, films with higher salt content exhibit a transient increase in storage modulus around 105 °C, possibly due to LiTFSI crystallization or the evaporation of trapped solvent, followed by a gradual decline as the temperature continues to rise. Figure 1b display the TGA curves of PVA/epoxy films containing different amounts of LiTFSI salt, demonstrating a four-phase decomposition pattern that is consistent across all samples: the initial drying phase (below 240 °C), the first decomposition stage (240–310 °C), the second decomposition stage (310–480 °C), and the final carbonization phase (above 480 °C). This four-stage decomposition closely resembles the thermal decomposition behavior of PVA polymer[46] and PVA/LiTFSI.[47] During the drying phase, the mass loss corresponds to the evaporation of solvent and moisture trapped in the material, with varying amounts depending on the LiTFSI salt concentration. The sample with 10 wt% LiTFSI salt showed a 10 wt% mass loss, while the samples with 20, 30, and 40 wt% LiTFSI salt exhibited mass losses of 13, 15, and 22 wt%, respectively. This trend indicates that increasing the LiTFSI salt concentration leads to greater retention of solvent and moisture, likely due to the hygroscopic nature of the salt or the increased complexity of the drying in compositions with higher salt content, which may enhance the potential for trapping more solvent. Keeping constant the LiTFSI-to-PVA/epoxy ratio of 4:6, different Al_2O_3 nanofiller concentrations (5, 10, 15, and 20 wt%) were tested, with their DMA and TGA results shown in Figure 1c,d. Figure 1c illustrates the storage modulus as a function of temperature for the PVA/epoxy/LiTFSI films with varying Al_2O_3 content. Increasing the Al_2O_3 content generally led to a higher storage modulus, indicating enhanced mechanical stiffness. However, the relative decrease in storage modulus with increasing temperature also became more pronounced, suggesting

© 2025 The Author(s). Advanced Energy and Sustainability Research published by Wiley-VCH GmbH

26999412, 0, Downloaded from https://advanced.onlinelibrary.wiley.com/doi/10.1002/aesr.202500222 by Universidade do Porto, Wiley Online Library on [21/10/2025]. See the Terms and Conditions (https://onlinelibrary.wiley.com/terms-and-conditions) on Wiley Online Library for rules of use; OA articles are governed by the applicable Creative Commons License

reduced thermomechanical stability under elevated thermal conditions. In detail, by adding 5 wt% Al_2O_3, the storage modulus increases to 33.6 MPa at room temperature but drops by 80% to 6.1 MPa upon heating to 150 °C. With 10 wt% Al_2O_3, the storage modulus of films increases to 41.7 MPa at room temperature and decreases by 82% to 7.2 MPa at 150 °C. At 15 wt% Al_2O_3, the storage modulus rises further to 56 MPa but experiences a similar 82% reduction, falling to 10 MPa at 150 °C. When the Al_2O_3 content is increased to 20 wt%, the modulus reaches 178 MPa but declines by 88%, dropping to 21 MPa at 150 °C. Having 20 wt% Al_2O_3 resulted in a significant increase in stiffness, with the storage modulus reaching 178 MPa at room temperature, nearly 18 times higher than that of the film without any nanofillers. At 150 °C, the modulus remained 2.5 times higher (21 MPa) than that of the films without Al_2O_3. Remarkably, the storage modulus of thin films with 20 wt% Al_2O_3 at high temperatures (150 °C) still exceeded the stiffness of the thin film without nanofiller at lower temperatures. The TGA results shown in Figure 1d reveal a consistent five-phase decomposition pattern across all samples: the initial drying phase (below 100 °C), the second drying phase (below 250 °C), the first decomposition stage (250–360 °C), the second decomposition stage (360–450 °C), and the final carbonization (above 450 °C). During the drying phase, mass losses of 28, 26, 21, and 25 wt% were observed, corresponding to the evaporation of solvent and moisture trapped in thin films containing 5, 10, 15, and 20 wt% nanofiller, respectively.

Ionic mobility is known to be enhanced by the segmental motion of the polymer host, with ionic conductivity occurring predominantly in amorphous regions of the material.[48,49] Here, DSC and XRD analyses (shown in **Figure 2**) were conducted to investigate how the amorphous phase evolves across different compositions. Figure 2a presents the DSC analysis of the final matrix- with the formulation of $PVA_{0.34}/epoxy_{0.14}/LiTFSI_{0.32}/(Al_2O_3)_{0.2}$— in comparison with neat epoxy, pure PVA, PVA/epoxy (with a ratio of 70:30), and PVA/epoxy/LiTFSI (with a LiTFSI-to-PVA/epoxy ratio of 40:60). The results showed that epoxy had a glass transition temperature (T_g) of 84 °C, with no melting point detected within the tested temperature range, consistent with the supplier's datasheet.[50] Pure PVA showed a T_g of 78 °C and a strong endothermic peak at 226 °C, corresponding to its melting point; literature reports a T_g of 87 °C and a melting point of 218.5 °C for pure PVA.[51] The PVA/epoxy blend demonstrated a slightly lower T_g of 73 °C and a melting point of 221 °C. Incorporating LiTFSI into the PVA/epoxy system further reduced the T_g to ≈42 °C and lowered the melting point to 162 °C. It has been widely reported that the addition of salts decreases the glass transition temperature. For instance, one study using LiTFSI and PVA with water as the solvent—with only 1% trapped solvent and 25 wt% salt concentration—observed a T_g of 58 °C.[47] In the present work, DMSO was used as the solvent, resulting in a higher residual solvent content of ≈13%, and a salt concentration of 40 wt% was used; both factors contributed to the lower observed T_g. The matrix, consisting of the PVA/epoxy/LiTFSI blended with 20 wt% Al_2O_3, exhibited a T_g near 46 °C, slightly higher than compositions without the nanofiller. These results indicate that the nanofiller increased the crystallinity of the polymer host, consistent with literature reports that the addition of fillers can enhance polymer crystallization.[35]

The XRD patterns (Figure 2b) further support these observations. Pure PVA exhibited the most prominent peak among the tested compositions at $2\theta = 19.5°$, corresponding to its orthorhombic lattice and semicrystalline nature, as reported in ref. [52]. Neat epoxy displayed a broad halo with very low-intensity features, characteristic of amorphous thermoset polymers.[53] When PVA was blended with epoxy, the peak intensity decreased compared to pure PVA, suggesting disruption of the PVA crystalline structure by epoxy. Further addition of LiTFSI continued to reduce crystallinity. However, the introduction of nanofillers in the matrix resulted in a sharper peak at $2\theta = 19.5°$, indicating partial recrystallization.

2.1.2. Electrochemical Results

Figure 3 visually compares PVA/epoxy polymer solutions with 40, 50, and 60 wt% LiTFSI. As shown in Figure 3b,c, both the 50 and 60 wt% concentrations exhibited phase separation during

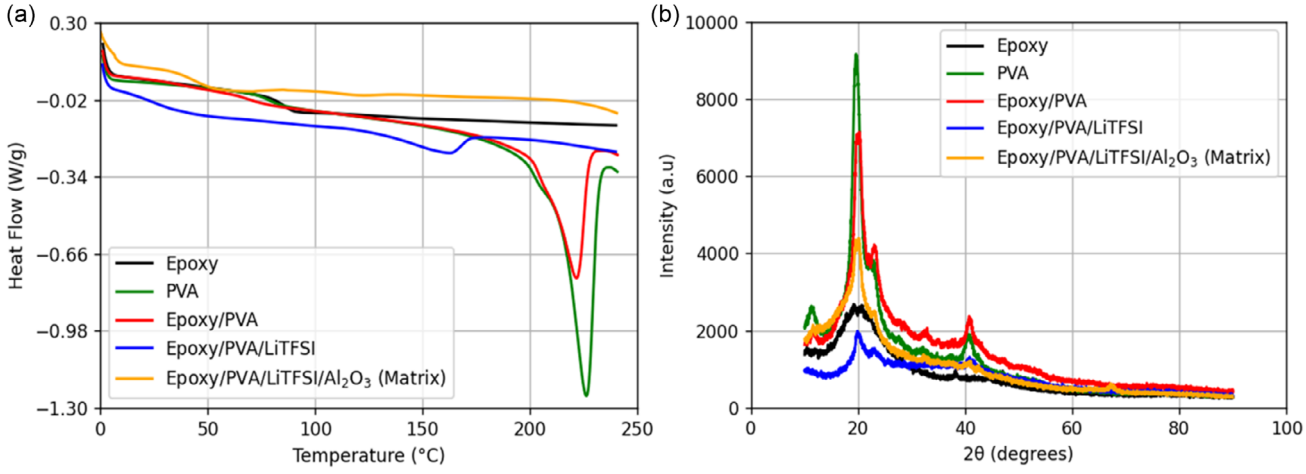


Figure 2. a) DSC and b) XRD of the matrix ($PVA_{0.34}/epoxy_{0.14}/LiTFSI_{0.32}/(Al_2O_3)_{0.2}$) compared with neat epoxy, pure PVA, PVA/epoxy, and PVA/epoxy/LiTFSI.

© 2025 The Author(s). Advanced Energy and Sustainability Research published by Wiley-VCH GmbH

26999412, 0, Downloaded from https://advanced.onlinelibrary.wiley.com/doi/10.1002/aesr.202500222 by Universidade do Porto, Wiley Online Library on [21/10/2025]. See the Terms and Conditions (https://onlinelibrary.wiley.com/terms-and-conditions) on Wiley Online Library for rules of use; OA articles are governed by the applicable Creative Commons License

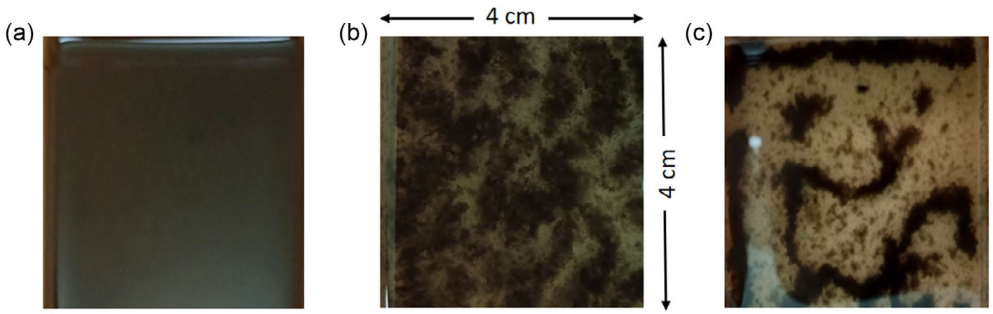


Figure 3. Schematic of the PVA/epoxy/LiTFSI solutions: a) LiTFSI: 40 wt%; b) LiTFSI: 50 wt%; c) LiTFSI: 60 wt%.

the drying stage. These results suggest that the salt concentration should not exceed 40 wt%.

The Nyquist plots obtained from PEIS tests of different thin films are shown in **Figure 4**. Figure 4a–d shows the results of PVA/epoxy samples with different concentrations of LiTFSI (10, 20, 30, and 40 wt%), measured at four temperatures (25, 50, 75, and 100 °C). The coefficient of variation (CV) for each dataset was calculated using the bulk resistance of each sample group at room temperature. The CV ranged from 5% to 10% across different compositions, indicating high repeatability. The results demonstrate that increasing the LiTFSI content leads to a decrease in resistance, with the 40 wt% sample showing the lowest bulk resistance. Moreover, increasing the temperature also reduces the overall resistance across all compositions. Considering that 40 wt% LiTFSI salt yielded the highest ionic conductivity without phase separation, the salt-to-PVA/epoxy ratio was maintained at 4:6 for the second part of the optimization, and the effect of different Al_2O_3 nanofiller concentrations (5, 10, 15, and 20 wt%) was assessed. The corresponding Nyquist plots at various temperatures (25, 50, 75, and 100 °C) are shown in Figure 4e–h. The CV for each dataset was calculated using the bulk resistance of each sample at room temperature. The values ranged from 3% to 15%, indicating high repeatability across different compositions.

The plots in Figure 4 display two distinct regions: 1) a high-frequency semicircle, which is assigned to the bulk properties of the electrolyte, and 2) an upward tilted straight line at low frequency, corresponding to the ion migration and electrode–electrolyte interfacial effects. The bulk resistance (R_b) of the polymeric films was determined by the intersection of the low-frequency end of the semicircle with the high-frequency end of the straight line along the real axis.[54,55] In films with lower resistance, such as those shown in Figure 4b–h, no semicircle is visible. Therefore, the bulk resistance was obtained from the

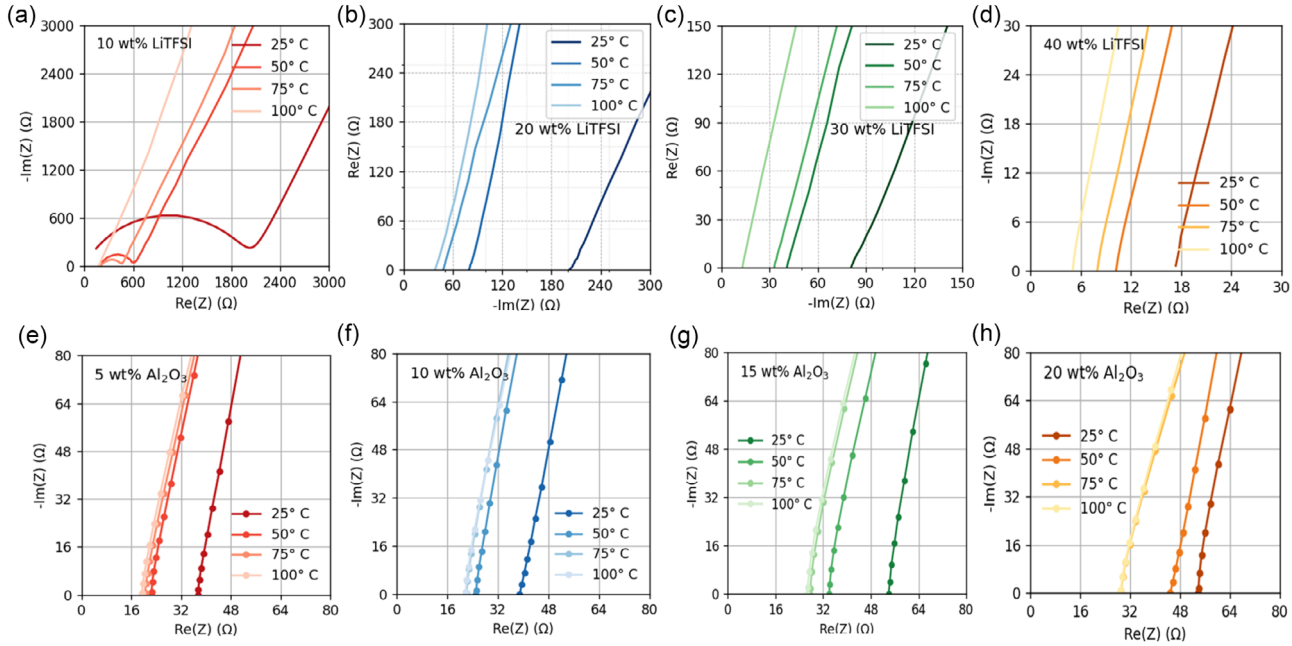


Figure 4. a–d) Nyquist plots of PVA/epoxy films with different concentrations of LiTFSI at different temperatures: (a) 10 wt% LiTFSI, (b) 20 wt% LiTFSI, (c) 30 wt% LiTFSI, (d) 40 wt% LiTFSI; e–h) Nyquist plot of PVA/epoxy/LiTFSI films with different amounts of Al_2O_3 at different temperatures: (e) 5 wt% Al_2O_3; (f) 10 wt% Al_2O_3; (g) 15 wt% Al_2O_3; (h) 20 wt% Al_2O_3.

© 2025 The Author(s). Advanced Energy and Sustainability Research published by Wiley-VCH GmbH

26999412, 0, Downloaded from https://advanced.onlinelibrary.wiley.com/doi/10.1002/aesr.202500222 by Universidade do Porto, Wiley Online Library on [21/10/2025]. See the Terms and Conditions (https://onlinelibrary.wiley.com/terms-and-conditions) on Wiley Online Library for rules of use; OA articles are governed by the applicable Creative Commons License

point where the impedance line intercepts the real axis. Eventually, the ionic conductivity (σ) of the polymer thin films can be calculated using Equation (1).

$$\sigma = \frac{t}{A \cdot R_b} \tag{1}$$

where A represents the electrode-thin film contact area, and t is the film thickness. Ionic conductivity values, expressed in S cm^{-1}, are presented in **Table 1**. The left side of the table shows the results of LiTFSI optimization, indicating that increasing the LiTFSI concentration enhances the ionic conductivity. For example, at room temperature, the conductivity at 10 wt% LiTFSI was 6.1×10^{-6} S cm^{-1}, which rose to 7.3×10^{-4} S cm^{-1} at 40 wt% LiTFSI. Additionally, the conductivity increases with temperature. For instance, at 20 wt% LiTFSI, it increased from 6.1×10^{-5} S cm^{-1} at 25 °C to 3.3×10^{-4} S cm^{-1} at 100 °C. The highest conductivity was observed at 40 wt% LiTFSI, where it ranged from 7.3×10^{-4} S cm^{-1} at 25 °C to 2.5×10^{-3} S cm^{-1} at 100 °C. Thus, both LiTFSI concentration and temperature showed a positive impact on ionic conductivity. The right side of Table 1 presents the ionic conductivity results for films containing different amounts of Al_2O_3 nanofiller at various temperatures, with the salt-to-PVA/epoxy ratio maintained at 4:6. The ionic conductivity values remained consistently in the range of 10^{-4} S cm^{-1}, indicating that the addition of nanofiller did not significantly alter the overall ionic conductivity; however, a slight negative effect can be observed with increasing Al_2O_3 content. For example, at room temperature, the results show that as the Al_2O_3 concentration increases from 5 to 20 wt%, the ionic conductivity decreases from 3.3×10^{-4} S cm^{-1} for 5 wt% nanofiller to 2.3×10^{-4} S cm^{-1} for 20 wt% nanofiller. Based on the literature, the addition of fillers can enhance polymer crystallization, leading to ion trapping and a subsequent decrease in ionic conductivity,[35] which aligns with the DSC and XRD results shown in Figure 2. In addition, with higher amounts of nanofiller, the total concentration of salt in the film decreases. While the ratio of salt-to-PVA/epoxy was kept constant at 4:6, at a lower nanofiller concentration, such as 5 wt%, the salt constitutes 38 wt% of the film. However, at 20 wt% nanofiller, the salt content reduces to 32 wt% of the film. This reduction in salt concentration likely contributed to the slight decrease in ionic conductivity as the nanofiller content increased. A similar trend is observed at higher temperatures. Consistently, for each nanofiller concentration, the ionic conductivity increased with rising temperature. For instance, in thin films with 5 wt% Al_2O_3, the ionic conductivity increased from 3.3×10^{-4} S cm^{-1} at 25 °C to 6.5×10^{-4} S cm^{-1} at 100 °C.

Table 1. Ionic conductivity of PVA/epoxy-based films with varying LiTFSI and Al_2O_3 content at different temperatures.

LiTFSI optimization			Al_2O_3 optimization		
LiTFSI [wt%]	T [°C]	σ [S cm^{-1}]	Al_2O_3 [wt%]	T [°C]	σ [S cm^{-1}]
10	25	6.1×10^{-6}	5	25	3.3×10^{-4}
10	50	2.1×10^{-5}	5	50	5.6×10^{-4}
10	75	2.7×10^{-5}	5	75	6.1×10^{-4}
10	100	7.2×10^{-5}	5	100	6.5×10^{-4}
20	25	6.1×10^{-5}	10	25	3.2×10^{-4}
20	50	1.6×10^{-4}	10	50	5.0×10^{-4}
20	75	2.6×10^{-4}	10	75	5.7×10^{-4}
20	100	3.3×10^{-4}	10	100	5.8×10^{-4}
30	25	1.6×10^{-4}	15	25	2.3×10^{-4}
30	50	3.1×10^{-4}	15	50	3.7×10^{-4}
30	75	3.8×10^{-4}	15	75	4.5×10^{-4}
30	100	9.6×10^{-4}	15	100	4.7×10^{-4}
40	25	7.3×10^{-4}	20	25	2.3×10^{-4}
40	50	1.3×10^{-3}	20	50	2.8×10^{-4}
40	75	1.6×10^{-3}	20	75	4.3×10^{-4}
40	100	2.5×10^{-3}	20	100	4.4×10^{-4}

Figure 5 shows the ionic conductivity of PVA/epoxy/LiTFSI and PVA/epoxy/LiTFSI/Al_2O_3 films at different temperatures.

2.1.3. Correlation and Summary

In summary, the results from PEIS, DMA, TGA, DSC, and XRD were found to correlate with one another. PEIS results showed that increasing the amount of salt decreases bulk resistance, thereby increasing ionic conductivity. However, DMA results revealed that salt has the opposite effect on mechanical properties due to plasticization: increasing salt content reduces mechanical stiffness. This was further supported by DSC and XRD analyses, which showed that the addition of salt lowers both the glass transition temperature and the crystallinity of the polymer film, both of which are commonly associated in the literature with enhanced ionic conductivity but reduced mechanical integrity. In addition, thin films with higher LiTFSI concentrations exhibited better thermomechanical stability, as evidenced by a smaller reduction in storage modulus at elevated temperatures.

Interestingly, this trend reversed upon the addition of nanofillers. PEIS and DMA results showed that nanofillers decrease ionic conductivity while enhancing mechanical properties. This observation was also consistent with DSC and XRD data, which indicated that the addition of nanofillers increases both T_g and crystallinity. Although increasing Al_2O_3 content improves the initial mechanical stiffness of the polymer films, as shown by a higher storage modulus, it also leads to a more significant decline in modulus with temperature, indicating reduced thermomechanical stability at elevated temperatures. Therefore, an optimal balance between salt concentration and nanofiller content is essential to achieve a favorable trade-off between ionic conductivity and mechanical stability.

2.2. Structural Electrolyte

2.2.1. Thermomechanical Results

The manufactured structural electrolyte had a thickness of 0.3 mm and a density of 0.02 g cm^{-3}. Compared to pure glass fiber, which has a density of 0.008 g cm^{-3}, this indicates ≈60 wt% polymer matrix. The mechanical, thermomechanical,

© 2025 The Author(s). Advanced Energy and Sustainability Research published by Wiley-VCH GmbH

26999412, 0, Downloaded from https://advanced.onlinelibrary.wiley.com/doi/10.1002/aesr.202500222 by Universidade do Porto, Wiley Online Library on [21/10/2025]. See the Terms and Conditions (https://onlinelibrary.wiley.com/terms-and-conditions) on Wiley Online Library for rules of use; OA articles are governed by the applicable Creative Commons License

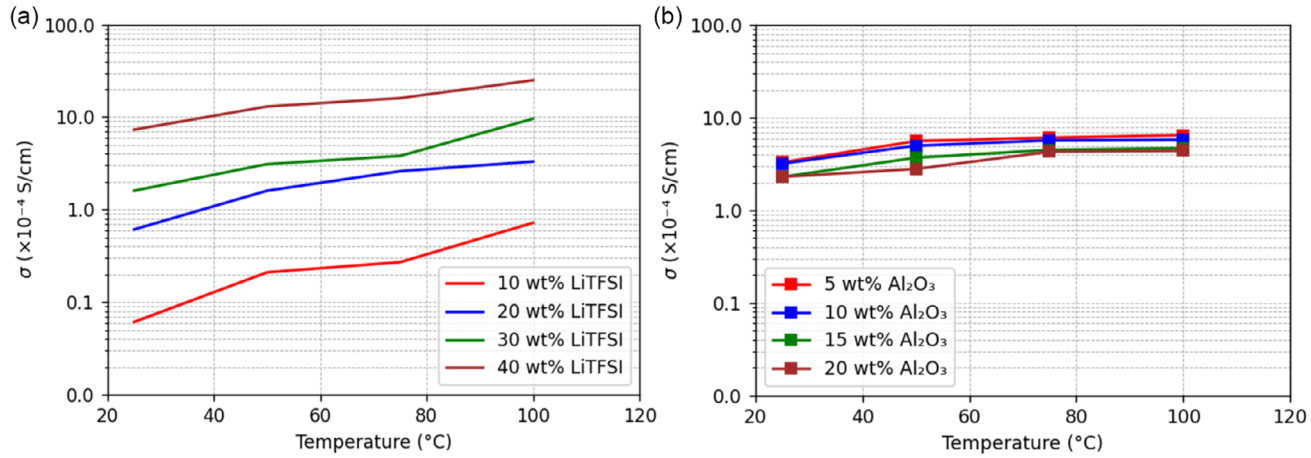


Figure 5. Ionic conductivity of thin films at different temperatures: a) PVA/epoxy/LiTFSI with different concentrations of LiTFSI; b) PVA/epoxy/LiTFSI/Al_2O_3 with different concentrations of Al_2O_3.

and thermal properties of the structural electrolyte are shown in **Figure 6**. Figure 6a demonstrates the good flexibility of the manufactured structural electrolyte, which showed no damage under hand-bending. The Universal tensile tester and stress–strain curves for three structural electrolyte films are shown in Figure 6b,c. As shown in Figure 6b, the fracture point consistently appeared in the middle of the thin films, away from the grip clamps. The stress–strain curves in Figure 6c show a CV of ≈3% for both the strain and stress axes, verifying the repeatability of the manufacturing and testing processes. The linear slope of these curves represents an average Young's modulus (bulk stiffness) of 1.82 GPa. The maximum stress corresponds to an average tensile strength of 56.9 MPa, and the average failure strain for the group of samples was 3.12%. The

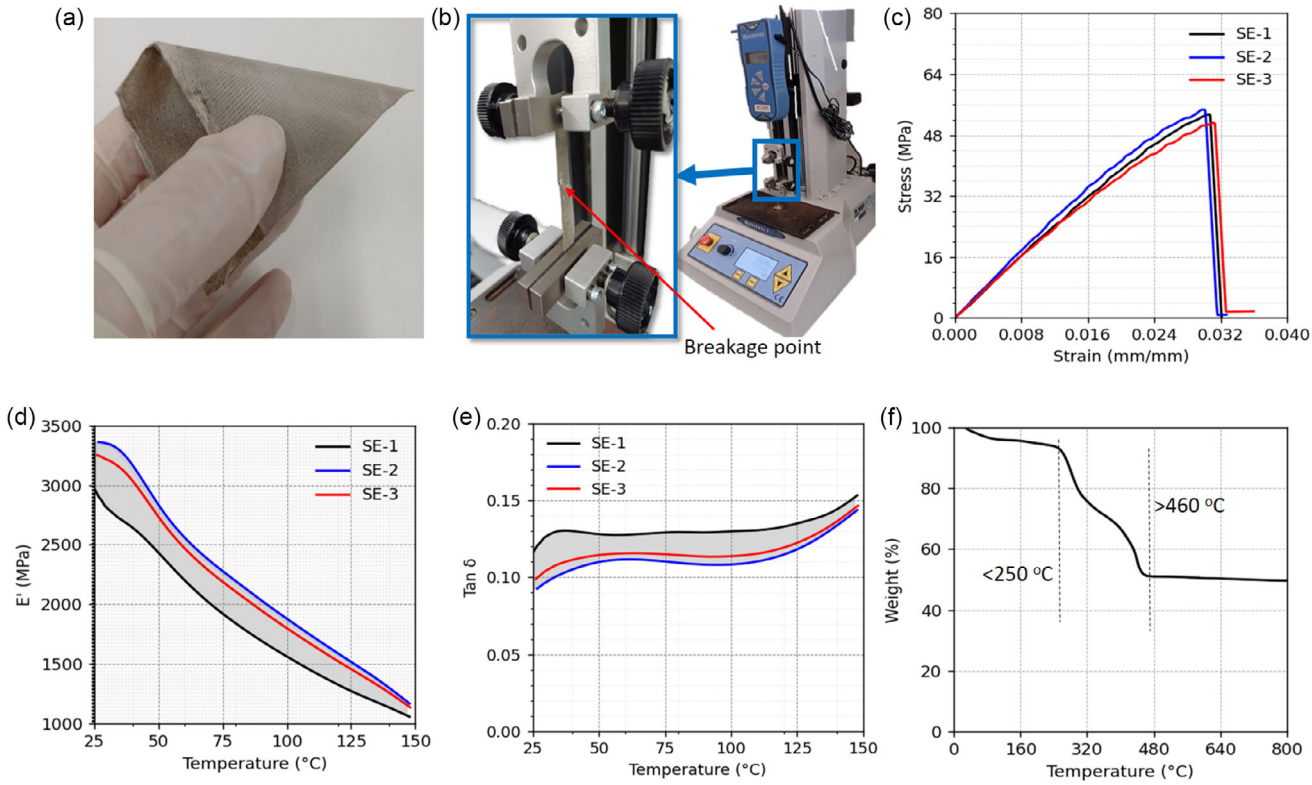


Figure 6. Mechanical, thermomechanical, and TGA results of the structural electrolyte (Glass fiber reinforced with $PVA_{0.34}$/$epoxy_{0.14}$/$LiTFSI_{0.32}$/$(Al_2O_3)_{0.2}$ matrix): a) Structural electrolyte under hand-bending; b) Universal tensile tester; c) Stress versus strain; d) Storage modulus (E'); e) Tan δ; f) TGA results.

© 2025 The Author(s). Advanced Energy and Sustainability Research published by Wiley-VCH GmbH

26999412, 0, Downloaded from https://advanced.onlinelibrary.wiley.com/doi/10.1002/aesr.202500222 by Universidade do Porto, Wiley Online Library on [21/10/2025]. See the Terms and Conditions (https://onlinelibrary.wiley.com/terms-and-conditions) on Wiley Online Library for rules of use; OA articles are governed by the applicable Creative Commons License

thermomechanical properties of the structural electrolyte are shown in Figure 6d,e. The CV of the three samples across different temperatures was ≈5%. Figure 6d illustrates the storage modulus of the structural electrolyte as a function of temperature. At room temperature, the average storage modulus was 3.2 GPa, decreasing to ≈1.1 GPa at 150 °C, representing a 65% reduction. Compared to the optimized composite polymer electrolyte, at room temperature, the storage modulus increased significantly from 178 MPa to 3 GPa, demonstrating more than a 16-fold improvement due to the inclusion of glass fiber. Comparing the results of Figure 6d at room temperature (25 °C) with the stiffness obtained from Figure 6c reveals that the storage modulus from the DMA test is higher than the bulk stiffness measured in the tensile test, which was found to be 1.82 GPa, ≈1.6 times lower than the storage modulus. This discrepancy arises from differences in sample size between the two tests and the testing methods. While DMA offers insights into molecular and microstructural dynamics, the tensile test assesses the overall bulk properties of the material. Some studies have attempted to correlate the results of these two tests.[56] Figure 6e displays tanδ versus temperature, representing the damping behavior of the structural electrolyte, which remained relatively stable across different temperatures. The value changed from 0.12 at room temperature to 0.15 at 150 °C. Figure 6f shows the TGA of the structural electrolyte, demonstrating a four-phase decomposition pattern: the initial drying phase (below 250 °C), the first decomposition stage (250–320 °C), the second decomposition stage (320–460 °C), and the carbonization phase (above 460 °C). This decomposition behavior closely resembles the thermal decomposition of glass fiber-reinforced epoxy, as reported in the literature.[57–59] Comparison of the TGA curve of the structural electrolyte with that of the composite polymer matrix (Figure 1d) reveals that the structural electrolyte exhibits higher thermal stability and resistance to heating, primarily due to the incorporation of glass fiber. The initial drying phase (below 250 °C) shows a 6 wt% mass loss, corresponding to the evaporation of solvent and moisture trapped in the structural electrolyte.

The microscopy images in **Figure 7** reveal distinct morphological differences among the pure PVA film, PVA/epoxy film, the matrix (PVA/epoxy/LiTFSI/Al_2O_3), and the structural electrolyte (glass fiber reinforced with the matrix). The pure PVA film (Figure 7a) shows a smooth, featureless surface, indicating a homogeneous structure with low porosity. Introducing epoxy (Figure 7b) results in microphase separation and a more complex, textured morphology. Further addition of LiTFSI and Al_2O_3 to the PVA/epoxy film—forming the matrix (Figure 7c)—increases heterogeneity and surface roughness due to multiphase interactions. In Figure 7d, the structural electrolyte appears more uniform and less phase-separated than the matrix. This may be attributed to the infiltration of the matrix into the glass fiber network, which could suppress surface phase contrast and smooth out visible heterogeneities.

2.2.2. Electrochemical Results

The overall electrochemical results of the structural electrolyte are shown in **Figure 8**. Figure 8a displays the Nyquist plots for one of the three tested samples at different temperatures in the Au@Al/SE/Au@Al pouch cell configuration. Although the structural electrolyte samples had a thickness of 0.3 mm, the Nyquist plots were normalized to a thickness of 0.5 mm to ensure comparability with the polymer films discussed in the previous section. The bulk resistance was obtained from the Nyquist plot using the same approach as for the polymer films, and the ionic conductivity of the membranes was calculated using Equation (1), and the results are shown in Figure 8b. The CV of the tested samples ranged between 4% and 7% across different temperatures. At room temperature, the average ionic conductivity was found to be 1.74×10^{-4} S cm^{-1}, which is still close to the value for the optimized composite electrolyte from the previous section (2.3×10^{-4} S cm^{-1}). Upon increasing the temperature to 50 °C, the ionic conductivity increased to 2.62×10^{-4} S cm^{-1}. Further heating to 75 and 100 °C resulted in conductivities of 3.8×10^{-4} and 5.9×10^{-4} S cm^{-1}, respectively. Figure 8c presents the Nyquist plot of the structural electrolyte in a half-cell cLFP/SE/Li configuration. The presence of two semicircles in the high- and mid-frequency regions corresponds to the resistance of the solid electrolyte interphase layer (R_{SEI}) and the charge-transfer resistance (R_{ct}) at the electrode/electrolyte interface, respectively. The relatively large diameter of the second semicircle indicates a high R_{ct}, suggesting sluggish electrochemical kinetics and interfacial polarization, likely contributing to the performance degradation. At low frequencies, the inclined line represents Warburg impedance, which reflects the diffusion of lithium ions within the electrode. The equivalent circuit of the cell was taken from[60] and is shown in the upper part of Figure 8b. The ionic conductivity of the cell can be calculated using Equation (1), with the total resistance being the sum

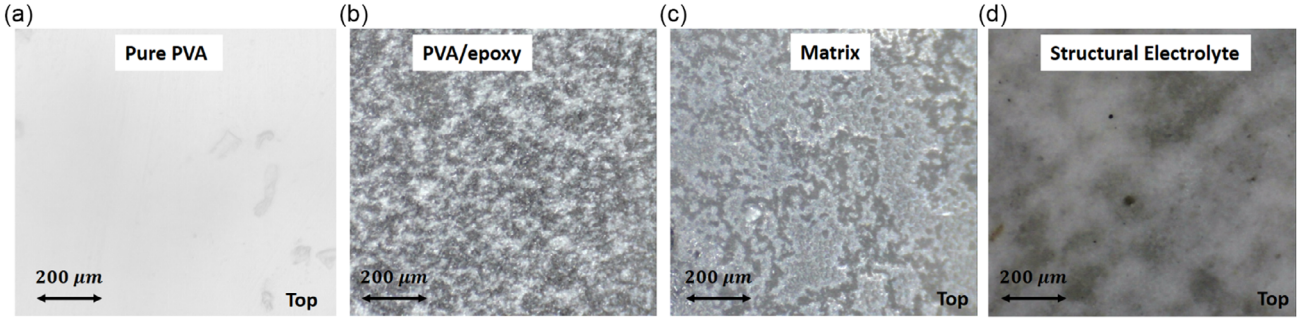


Figure 7. Microscopy images: a) Pure PVA; b) PVA/epoxy; c) Matrix ($PVA_{0.34}$/$epoxy_{0.14}$/$LiTFSI_{0.32}$/$(Al_2O_3)_{0.2}$); d) Structural electrolyte (Glass fiber reinforced with the matrix).

© 2025 The Author(s). Advanced Energy and Sustainability Research published by Wiley-VCH GmbH

26999412, 0, Downloaded from https://advanced.onlinelibrary.wiley.com/doi/10.1002/aesr.202500222 by Universidade do Porto, Wiley Online Library on [21/10/2025]. See the Terms and Conditions (https://onlinelibrary.wiley.com/terms-and-conditions) on Wiley Online Library for rules of use; OA articles are governed by the applicable Creative Commons License

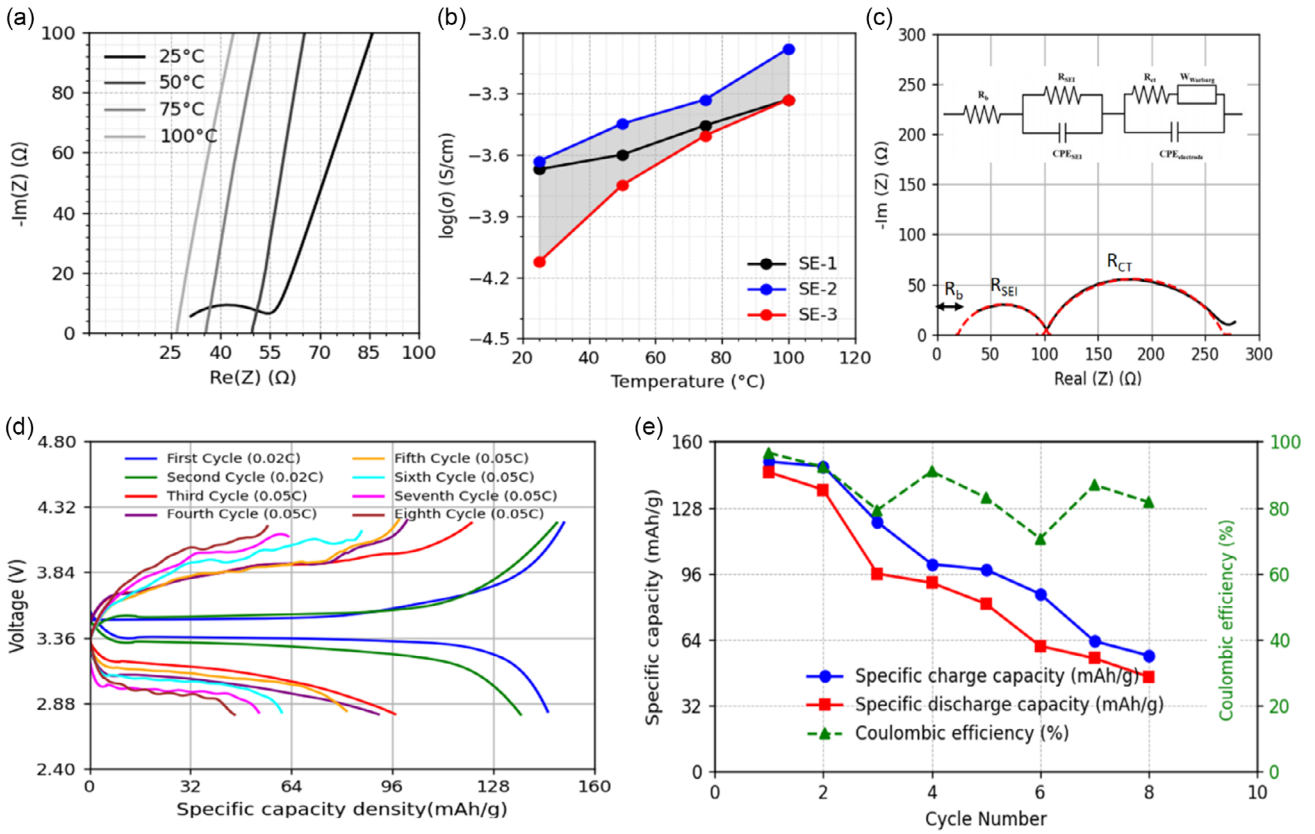


Figure 8. Electrochemical results of the structural electrolyte (glass fiber reinforced with $PVA_{0.34}/epoxy_{0.14}/LiTFSI_{0.32}/(Al_2O_3)_{0.2}$ matrix): a) Nyquist plots in symmetric Au@Al/SE/Au@Al configuration; b) Ionic conductivity in symmetric Au@Al/SE/Au@Al configuration; c) Nyquist plot in half-cell cLFP/SE/Li configuration; d) Voltage vs specific capacity of different cycles of the half-cell; e) Specific capacity of charge and discharge of the half-cell.

of the bulk resistance (R_b), R_{SEI}, and R_{ct}.[60] The calculated ionic conductivity is 6.3×10^{-5} S cm^{-1}.

Figure 8d shows the galvanostatic charge-discharge voltage profiles of the half-cell (cLFP/SE/Li) at different cycles and current rates. The first and second cycles were conducted at a lower current rate (0.02 C), while subsequent cycles were measured at 0.05 C. The initial discharge capacity reaches ≈150 mAh g^{-1}, indicating good initial electrochemical activity. However, as cycling progresses, both the charge and discharge capacities decrease noticeably, indicating a decline in capacity retention. The shape of the voltage profiles remains fairly stable in the early cycles, suggesting consistent electrochemical reactions, but the fading plateau region and shrinking capacity reflect increasing polarization and potential degradation of the electrode material over time. Figure 8e summarizes the cycling performance of the half-cell (cLFP/SE/Li) over eight charge-discharge cycles. The specific charge and discharge capacities decline progressively. Initially, the cell delivers a high charge capacity (≈150 mAh g^{-1}) and discharge capacity (≈145 mAh g^{-1}), indicating good electrochemical activity. However, both charge and discharge capacities decline over successive cycles, with the discharge capacity dropping to below 46 mAh g^{-1} by the eighth cycle. The Coulombic efficiency, calculated as the ratio of discharge to charge capacity density for each cycle,[61,62] remains moderate, fluctuating between ≈70% and 96%, suggesting that a portion of the charge is consistently lost to irreversible side reactions such as electrolyte decomposition or continuous SEI growth.

The electrochemical performance of the full cell comprising a custom-made LFP-coated aluminum foil, structural electrolyte, and custom-made graphite-coated copper foil in coin cell configuration is shown in **Figure 9**. Figure 9a displays the Nyquist plot of the cell, which reveals a bulk resistance of 22 Ω, a solid electrolyte interphase resistance of 17 Ω, and a charge-transfer resistance of 14 Ω, resulting in a total resistance of 53 Ω. The ionic conductivity for this configuration was calculated using Equation (1) to be 3.2×10^{-4} S cm^{-1}. Figure 9b illustrates the voltage versus capacity density over 240 cycles at various current rates. The battery was initially cycled at 0.02 C for two cycles, followed by six cycles at 0.05 C, six cycles at 0.1 C, ten cycles at 0.2 C, ten cycles at 0.5 C, and ten cycles at 1 C. It was then returned to 0.1 C for six cycles before undergoing long-term cycling at 1 C for an additional 185 cycles. This sequence-reducing the current rate after high-rate cycling, was designed to evaluate the reversibility of the electrochemical behavior and determine whether the cell could recover its capacity. The battery was charged and discharged between 0 and 2 V, which is lower than the operating voltage range for commercial LFP/graphite cells. At 0.02 and

© 2025 The Author(s). Advanced Energy and Sustainability Research published by Wiley-VCH GmbH

26999412, 0, Downloaded from https://advanced.onlinelibrary.wiley.com/doi/10.1002/aesr.202500222 by Universidade do Porto, Wiley Online Library on [21/10/2025]. See the Terms and Conditions (https://onlinelibrary.wiley.com/terms-and-conditions) on Wiley Online Library for rules of use; OA articles are governed by the applicable Creative Commons License

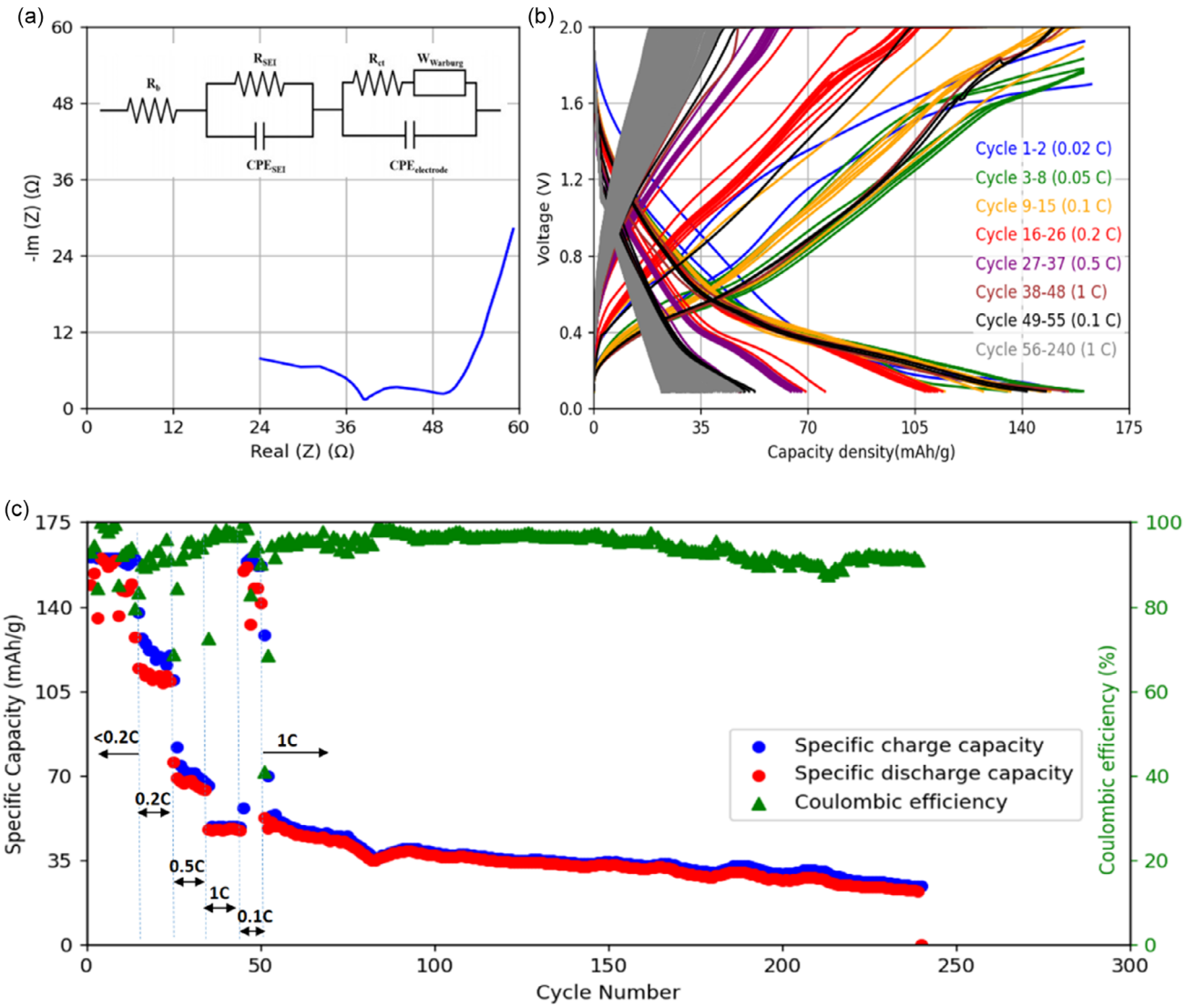


Figure 9. Electrochemical results of the structural electrolyte (glass fiber reinforced with a $PVA_{0.34}$/$epoxy_{0.14}$/$LiTFSI_{0.32}$/$(Al_2O_3)_{0.2}$ matrix) in the LFP/SE/G full cell configuration: a) Nyquist plots; b) Voltage vs. specific capacity for different cycles; c) Cycle number vs. Specific capacity of charge and discharge, and Coulombic efficiency.

0.05 C, the cell exhibited a charge capacity of ≈160 mAh g^{-1} and a discharge capacity of 155 mAh g^{-1}. At 0.1 C, the charge capacity remained around 160 mAh g^{-1}, while the discharge capacity decreased to ≈145 mAh g^{-1}. As the rate increased to 0.2 C, the charge and discharge capacities dropped to 124 and 110 mAh g^{-1}, respectively. Further increases in current rate to 0.5 and 1 C led to a progressive reduction in capacity, with the charge/discharge capacities declining to 72/67 and 50/47 mAh g^{-1}, respectively. To test reversibility, the cell was re-evaluated at 0.1 C, where it delivered a charge capacity of ≈158 mAh g^{-1} and a discharge capacity of 145 mAh g^{-1}, values closely matching those obtained earlier at 0.1 C results. This indicates good reversibility of the cell's electrochemical performance. Figure 9c shows the long-term cycling performance at 1 C over 180 cycles, where the charge and discharge capacities remained consistently close, demonstrating excellent cycling stability. Overall, the results indicate that the battery exhibits stable and repeatable behavior across different charge/discharge rates. As expected for solid-state batteries, capacity decreased with increasing current rate. Although the capacity retention declined to around 20% after 240 cycles, the Coulombic efficiency remained ≈95% throughout the tests, indicating high electrochemical reversibility and stable cyclability of the cell. To place these results in context, some recent studies are highlighted. In one study, PEO/LiTFSI/LLZTO solid electrolytes were used in a $Li/LiFePO_4$ cell configuration, achieving a high capacity of 155.2 mAh g^{-1} at 0.5 C and 45 °C, with a capacity retention of 84.3% after 500 cycles.[63] The superior electrochemical performance of that system, compared to the current study, is attributed to the use of the PEO-based electrolyte, which—when

© 2025 The Author(s). Advanced Energy and Sustainability Research published by Wiley-VCH GmbH

26999412, 0, Downloaded from https://advanced.onlinelibrary.wiley.com/doi/10.1002/aesr.202500222 by Universidade do Porto, Wiley Online Library on [21/10/2025]. See the Terms and Conditions (https://onlinelibrary.wiley.com/terms-and-conditions) on Wiley Online Library for rules of use; OA articles are governed by the applicable Creative Commons License

combined with LiTFSI—has a glass transition temperature of ≈−40 °C and was tested at 45 °C. The combination of a polymer with a low glass transition temperature and testing at elevated temperature enhanced ionic conductivity and charge/discharge capacity. Other studies have also reported similarly superior results.[36,64,65] Although not explicitly discussed in these studies, the testing conditions suggest that mechanical properties were likely not the primary focus. In comparison, the current study focuses on both mechanical properties and energy storage functionality at room temperature, which is desirable for structural batteries. To achieve enhanced mechanical properties, a PVA-based polymer system was employed. When combined with epoxy and LiTFSI, this system exhibited a glass transition temperature of 42 °C, considerably higher than that of the PEO systems. Additionally, the system was tested at room temperature (18–22 °C), which is typical for structural battery operation. Therefore, the lower capacity retention observed in the current study is expected, given the focus on mechanical robustness alongside electrochemical performance.

The overall results of the structural electrolyte, including the ionic conductivity (σ), bulk stiffness (E), tensile strength (σ_u), failure strain (ϵ), storage modulus (E'), Tan δ, and amount of trapped solvent (TS), are compiled in **Table 2**. The high mechanical properties, along with good ionic conductivity, demonstrate that the optimized structural electrolyte provides excellent multifunctionality, making it suitable for use in load-bearing energy-storage devices. Compared to Zhang et al.[66] who developed glass fiber reinforced with polyethylene oxide (PEO)/ionic liquid and achieved an ionic conductivity of 1.6×10^{-4} S cm^{-1} with 25 wt% ionic liquid, the current work reports a slightly higher ionic conductivity (1.74×10^{-4} S cm^{-1}) due to using a higher amount of LiTFSI salt compared to the amount of ionic liquid. However, their method does not result in a fully solid-state electrolyte, whereas the current approach achieves a fully solid-state electrolyte with only 6 wt% trapped solvent. Zhang et al. obtained a tensile strength of 36 MPa and stiffness of 0.81 GPa, while the current method achieves a higher tensile strength of 56.9 MPa and stiffness of 1.82 GPa. In another work, Dong et al.[67] manufactured a structural electrolyte using PEO, LiTFSI, LATP fillers, and glass fiber. They obtained a stiffness of around 1.2 GPa, a tensile strength of 33.1 MPa, and an ionic conductivity of 6.3×10^{-5} S cm^{-1}, which shows that both the mechanical properties and ionic conductivity of the current methodology are higher than in their work. These results confirm the suitability of the current optimized electrolyte for applications requiring high ionic conductivity and good mechanical properties across varying temperatures.

Table 2. The electromechanical properties of the structural electrolyte (glass fiber reinforced with $PVA_{0.34}$/$epoxy_{0.14}$/$LiTFSI_{0.32}$/$(Al_2O_3)_{0.2}$ matrix).

T [°C]	σ [S cm^{-1}]	E [GPa]	σ_u [MPa]	ϵ [%]	E' [GPa]	Tan δ	TS [wt%]
25	1.74×10^{-4}	1.82	56.9	3.12	3.2	0.113	6
50	2.6×10^{-4}	–	–	–	2.6	0.129	6
75	3.8×10^{-4}	–	–	–	2.1	0.129	6
100	5.9×10^{-4}	–	–	–	1.74	0.129	6

3. Conclusions

In this study, a structural electrolyte with remarkable mechanical properties and high ionic conductivity was successfully developed for load-bearing energy-storage applications, such as structural batteries. A composite matrix with the formulation $PVA_{0.34}$/$epoxy_{0.14}$/$LiTFSI_{0.32}$/$(Al_2O_3)_{0.2}$ was optimized and subsequently used to reinforce glass fibers, forming the structural electrolyte. The salt and nanofiller optimization results from PEIS, DMA, TGA, DSC, and XRD correlated with each other and collectively demonstrated a clear trade-off between ionic conductivity and mechanical stiffness in the composite matrix. While increasing salt content enhanced ionic conductivity by reducing bulk resistance, it compromised mechanical properties due to plasticization, as reflected in lower stiffness, reduced T_g, and crystallinity. Conversely, the addition of nanofiller reversed this trend-improving mechanical properties but reducing ionic conductivity by increasing both T_g and crystallinity. Notably, although nanofillers boost initial stiffness, they also decrease thermomechanical stability. These findings highlight the need for an optimized balance of salt and nanofiller concentrations to achieve desirable electrochemical and mechanical performance in CPEs. The structural electrolyte exhibited a bulk stiffness of 1.82 GPa, a tensile strength of 56.91 MPa, a failure strain of 0.0312, and a high ionic conductivity of 1.74×10^{-4} S cm^{-1} at room temperature. Additionally, it demonstrated a storage modulus of 3 GPa, a remarkable 16-fold improvement compared to the composite polymer electrolyte alone. Furthermore, the electrolyte maintained stable damping characteristics over a wide temperature range, from room temperature to 150 °C. Electrochemical testing in a lithium iron phosphate (LFP) half-cell showed good initial performance with high initial charge and discharge capacity densities. The full cell of the structural electrolyte, paired with custom-made LFP and graphite electrodes, demonstrated long cycle life and good cyclability for ≈240 cycles, maintaining a high Coulombic efficiency of 95% throughout. Both charge and discharge capacity densities decreased with increasing C-rate, which is typical behavior for solid-state electrolytes.

4. Experimental Section

Materials: In this study, the matrix part of the structural electrolyte consisted of a blend of PVA, epoxy, LiTFSI salt, and Al_2O_3 nanofiller. The PVA had a molecular weight between 146 000 and 186 000, with a purity greater than 99.3%, and was sourced from Thermo Scientific. DMSO solvent, acquired from Labkem, was used to dissolve the polymer and mix the different additives. The epoxy AS-89, supplied by HBQUIMICA, was a two-component system: Part A served as the resin, and Part B as the hardener, with a recommended mixing ratio of 100:45, according to the supplier's datasheet. The LiTFSI salt, with a purity of 99%, was obtained from Acros Organics, while the Aluminum oxide (Al_2O_3) nanofiller (flash grade), with a particle size of 18–32 microns and a molecular weight of 101.96 g mol^{-1}, was supplied by Thermo Scientific. For the separator, a plain-weave glass fiber with a [0/90]° orientation, a ply thickness of 70 µm, and an areal weight of 0.008 g cm^{-2} was used. The commercial cathode foil, consisting of an aluminum substrate coated with lithium iron phosphate (LFP), was obtained from MTI Corporation. The foil had a total thickness of 84 µm and an areal density of ≈13.5 mg cm^{-2}, comprising 95.4% LFP by weight, with the remaining content consisting of polyvinylidene fluoride (PVDF) and conductive carbon. LFP powder with an average particle size of

© 2025 The Author(s). Advanced Energy and Sustainability Research published by Wiley-VCH GmbH

26999412, 0, Downloaded from https://advanced.onlinelibrary.wiley.com/doi/10.1002/aesr.202500222 by Universidade do Porto, Wiley Online Library on [21/10/2025]. See the Terms and Conditions (https://onlinelibrary.wiley.com/terms-and-conditions) on Wiley Online Library for rules of use; OA articles are governed by the applicable Creative Commons License

1.5 µm was procured from MSE Supplies. Graphite powder and conductive acetylene black (Super P) were sourced from Nanografi. The PVDF binder was also obtained from MTI Corporation. All components used to assemble the 2032 coin cells—including the positive case, negative case, spring, and spacer—were supplied by Nanografi.

Manufacturing Thin Films and the Structural Electrolyte: In this study, a two-step progressive optimization process was conducted to identify the ideal matrix formulation. First, the optimal concentration of LiTFSI salt was determined to obtain desirable thermomechanical and electrochemical properties, using various characterization techniques. This optimal salt concentration was then used to establish the appropriate amount of Al_2O_3 nanofiller, employing the same evaluation methods. The modified solution casting technique presented in ref. [14] was used to fabricate the cells for PEIS tests. This method was introduced to address the poor interfacial contact between electrodes and thin films by incorporating a modified approach: the initial fabrication of thin films using the conventional solution casting technique was followed by a wetting step with the same polymer solution composition, and in situ drying of the film within the cell. These additional steps were intended to enhance electrode–electrolyte adhesion and improve interfacial contact.

For the polymer host preparation, PVA was dissolved in DMSO at 100 °C for 6 h using a magnetic stirrer set to 400 RPM. For the epoxy preparation, parts A and B were mixed in a 100:45 ratio, in compliance with the supplier's recommendation, and then combined with the polymer solution in a 30:70 ratio, excluding the solvent weight. The mixture was stirred for 10 min to ensure a homogeneous solution. In the first part of optimization, different percentages of LiTFSI salt (10%, 20%, 30%, 40%, and 50%) were mixed with the polymer solution using a magnetic stirrer at 60 °C and 400 RPM for 1 h. The resulting solutions were poured into silicone molds and dried in a vacuum heat chamber at 80 °C for three days before testing.

For compositions containing nanofillers, the previously prepared solution (using the best percentage of LiTFSI salt) was further modified by adding different percentages of Al_2O_3 (5%, 10%, 15%, and 20%). The solution was stirred for an additional 20 min to ensure uniform dispersion of the nanofiller. To prevent alumina from depositing during the drying stage, it was crucial to minimize the solvent usage, keeping it below 80%. The polymer dissolution process was conducted at 150 °C, with gradual addition of PVA to the solvent to ensure effective dissolution using less solvent. The resulting solutions were poured into silicone molds and dried in a vacuum heat chamber at 80 °C for three days, after which the films were tested accordingly. The optimized amounts of LiTFSI salt and Al_2O_3 nanofiller were then used to manufacture the structural electrolyte. This electrolyte was prepared using the PVA/epoxy polymer host in a 7:3 ratio, the optimized amounts of LiTFSI salt and Al_2O_3 nanofiller, and a single layer of plain-weave glass fiber with a [0/90]° orientation and a thickness of 70 µm. A layer of glass fiber was placed on a silicone mold, and the prepared polymer solution was poured over it. The assembly was dried according to the same procedure as the thin films. The general schematic of the method for optimizing composite polymer matrix and structural electrolyte is shown in **Figure 10**. Step 2 was applied only for PEIS tests to improve the contact between electrodes and the electrolyte. In the following subsections, the techniques used to evaluate the polymer matrix and structural electrolyte were explained.

Potentiostatic Electrochemical Impedance Spectroscopy Test: To perform the potentiostatic electrochemical impedance spectroscopy (PEIS) test, the thin films were first dried and then wetted on both sides with a solution matching their composition. They were subsequently assembled with the electrodes, which consisted of two aluminum sheets (20 × 20, 0.5 mm thick) coated with a 60 nm layer of gold to prevent potential reactions between the aluminum and the electrolyte during drying and testing. The assembly was then dried inside a vacuum chamber at 80 °C for 24 h. Electrochemical impedance measurements were conducted using a Biologic VMP-300 potentiostat. Nyquist plots of the thin films were generated through AC impedance spectroscopy, with data analysis carried out using EC-Lab

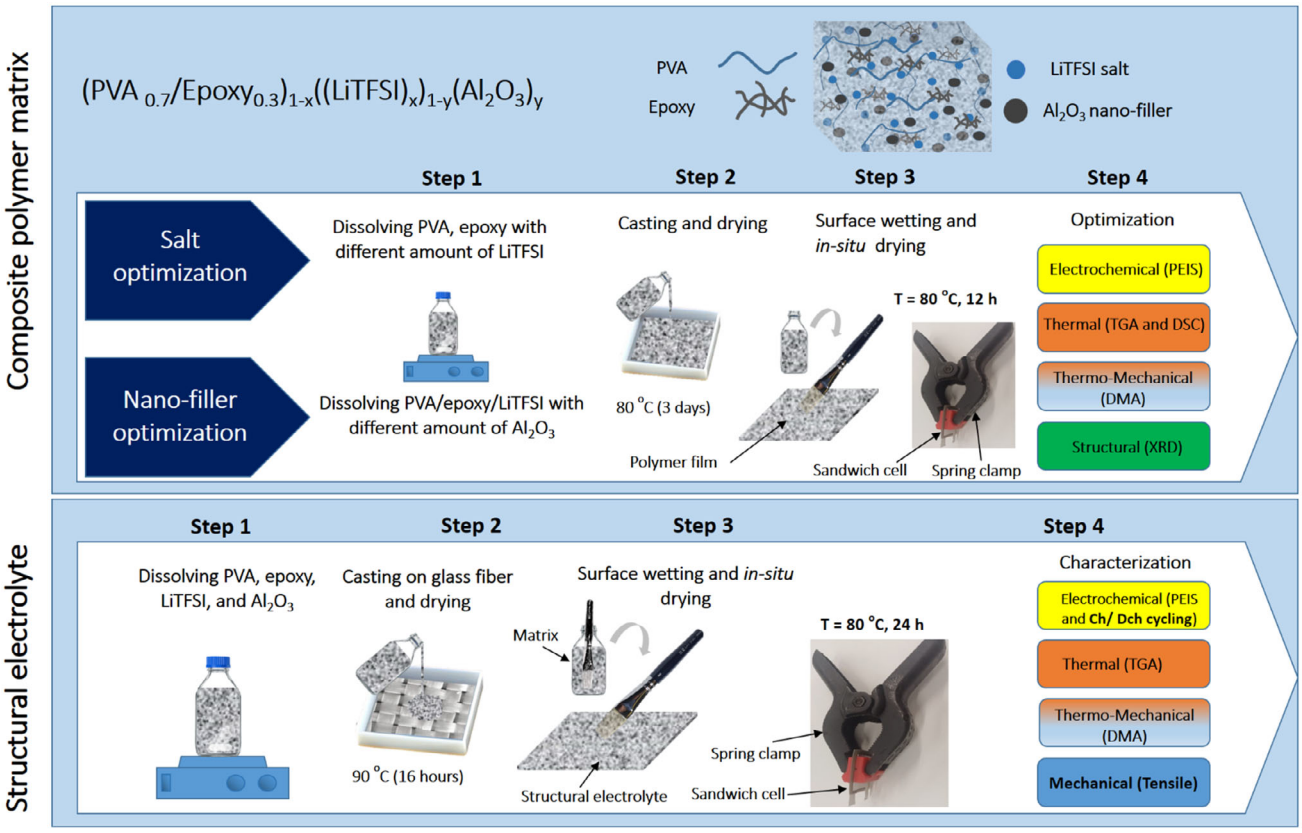


Figure 10. Schematics of the method for optimization of composite polymer matrix and manufacturing the structural electrolyte.

© 2025 The Author(s). Advanced Energy and Sustainability Research published by Wiley-VCH GmbH

26999412, 0, Downloaded from https://advanced.onlinelibrary.wiley.com/doi/10.1002/aesr.202500222 by Universidade do Porto, Wiley Online Library on [21/10/2025]. See the Terms and Conditions (https://onlinelibrary.wiley.com/terms-and-conditions) on Wiley Online Library for rules of use; OA articles are governed by the applicable Creative Commons License

V11.52 software. All impedance spectra presented in this study were recorded between the working/sense electrode (one of the coated aluminum electrodes) and the counter/reference electrode (the other coated aluminum electrode). PEIS tests were performed with a 10 mV amplitude relative to the electrochemical open circuit voltage, across frequencies ranging from 7 MHz to 1 Hz. Three samples were tested for each configuration to assess the repeatability of the methodology. Since the thin films had slight variations in thickness, the measured Nyquist plots were normalized to a standard film thickness of 0.5 mm for comparison. Accordingly, both the real and imaginary components of the impedance were multiplied by the factor 0.5/(thickness of film in mm).

Dynamic Mechanical Analysis: DMA tests were conducted using the HITACHI DMA7100 tester, in tension mode, with temperatures from 25 up to 150 °C. The tests were performed at a frequency of 1 Hz and a heating rate of 5 °C min^{-1}. The sinusoidal oscillation amplitude was set to 10 µm. Three samples were tested for each configuration to assess the repeatability of the methodology. The thin films measured 12 mm in length, 6 mm in width, and had a thickness between 0.5 and 1 mm. Each rectangular sample was clamped in the sample holder and tightened to 3 N m using a calibrated torque wrench at room temperature.

Thermogravimetric Analysis: TGA were conducted using a HITACHI STA300 instrument to assess trapped solvents and moisture absorption in each composition. Testing was performed in a platinum pan, with the temperature gradually increasing from 30 to 800 °C at a rate of 10 °C min^{-1}. A constant nitrogen gas flow of 100 mL min^{-1} was maintained throughout the process.

Differential Scanning Calorimetry: DSC analyses were conducted using a Q20 model calorimeter (TA Instruments) to determine heat flow, glass transition temperature, and melting point. Samples were tested in aluminum pans, with the temperature gradually increased from 0 to 240 °C at a rate of 10 °C min^{-1}. A constant nitrogen gas flow of 50 mL min^{-1} was maintained throughout the process. All samples had a weight of ≈9 mg.

X-ray Diffraction: XRD measurements were carried out using a PANalytical Empyrean diffractometer equipped with a Cu anode ($K_\alpha = 1.5406$ Å) operating at 30 kV and 55 mA. Scans were performed in reflection-transmission mode over a 2θ range of 10°–90° with a step size of 0.026° using a continuous scan mode. A fixed divergence slit of 0.38 mm was used, and no monochromator was applied. Calibration offsets were applied to 2θ (−0.016°) and Omega (+0.0397°).

Tensile Test: Quasistatic tensile tests of the structural electrolyte were performed following the ASTM D882 standard test method using a Mecmesin Universal Tensile Tester with a 1 kN load cell limit to evaluate the mechanical properties of the structural electrolyte, specifically the stiffness, tensile strength, and failure strain. The tests were conducted at a rate of 1 mm min^{-1}. To evaluate the repeatability of the methodology, three samples were tested for each configuration. All samples were rectangular, with approximate dimensions of 8 mm in width, 0.3 mm in thickness, and 80 mm in length, with a grip-to-grip distance of 60 mm. The tensile tester recorded load versus time. Strain was directly determined using the crosshead displacement.

Charge/discharge Test: The electrochemical performance of the structural electrolyte was evaluated in both half-cell and full-cell configurations. For the half-cell configuration, a 2032 coin cell was assembled using a commercial LFP foil as a cathode, the structural electrolyte, and a lithium metal anode. This configuration is hereafter referred to as cLFP/SE/Li. Both manufacturing and testing were performed at room temperature (18–22 °C). The cathode was cut with a diameter of 15 mm, resulting in an active LFP mass of 22.6 mg. Based on this mass and the manufacturer's specified cathode specific capacity of 150 mAh g^{-1}, the currents for different charge/discharge rates were calculated accordingly. The charge/discharge cycle tests were conducted using a Neware CT-4008Tn-5V20mA-164 battery cycler (Neware, Shenzhen, China). Each cycle consisted of constant current–constant voltage charging, a 1 min rest, constant voltage discharging, and another rest period. The upper and lower cutoff voltages were set to 4.2 and 2.8 V, respectively, in accordance with the literature.[68] In the full-cell configuration with custom-made electrodes, aluminum and copper foils were cut into 15 mm diameter discs and subsequently coated with LFP and graphite slurries, respectively. The coated foils were dried at 45 °C for 12 h. After drying, the manufactured LFP foil had an areal density of 3 mg cm^{-2} (80% LFP, 10% PVDF, 10% conductive carbon by weight). Structural electrolyte films were cut into 18 mm diameter discs. Following the modified solution casting technique, both sides of the electrolyte were wetted with the matrix solution before being assembled between the LFP and graphite electrodes. The resulting stack was clamped with a single spring clamp (0.7 bar) to ensure good contact and dried in a vacuum chamber at 45 °C for 20 h. After drying, the assembled layers were transferred to a glovebox for final coin cell assembly. Since the electrode foils had low thicknesses (less than 0.1 mm), two springs were used in the coin cell to ensure proper contact between the central active components. This configuration is hereafter referred to as LFP/SE/G.

Acknowledgements

The authors would like to acknowledge the support of the Portuguese Foundation for Science and Technology under the FCT grant for the UIDP/50022/2020 LAETA project. Additionally, Maryam Niazi expresses gratitude to LAETA and FCT for the doctoral scholarship UI/BD/151558/2021. This work also received support through FCT/MCTES (PIDDAC) for LEPABE (UIDB/00511/2020; UIDP/ 00511/2020) and ALiCE (LA/P/0045/2020).

Conflict of Interest

The authors declare no conflict of interest.

Data Availability Statement

The data that support the findings of this study are available from the corresponding author upon reasonable request.

Keywords

composite polymer electrolytes, energy storage, glass fiber, structural batteries, structural electrolytes

Received: May 30, 2025
Revised: September 8, 2025
Published online:

[1] L. E. Asp, K. Bouton, D. Carlstedt, S. Duan, R. Harnden, W. Johannisson, M. Johansen, M. K. G. Johansson, G. Lindbergh, F. Liu, K. Peuvot, L. M. Schneider, J. Xu, D. Z. Peuvot, L. M. Schneider, J. Xu, D. Zenkert, *Adv. Energy Sustainability Res.* **2021**, *2*, 2000093.
[2] M. Niazi, F. Danzi, D. Dalli, P. P. Camanho, *Compos. Struct.* **2025**, *364*, 119053.
[3] F. Danzi, R. M. Salgado, J. E. Oliveira, A. Arteiro, P. P. Camanho, M. H. Braga, *Molecules* **2021**, *26*, 2203.
[4] D. Carlstedt, E. Marklund, L. E. Asp, *Compos. Sci. Technol.* **2019**, *169*, 26.
[5] X. Yu, A. Manthiram, *Adv. Energy Sustainability Res.* **2021**, *2*, 2000102.
[6] M. S. Siraj, S. Tasneem, D. Carlstedt, S. Duan, M. Johansen, C. Larsson, J. Xu, F. Liu, F. Edgren, L. E. Asp, *Adv. Energy Sustainability Res.* **2023**, *4*, 2300109.
[7] R. Tavano, M. Spagnol, R. J. Nawres Al-Ramahi, J. Xu, L. E. Asp, *Polymer* **2024**, *312*, 127646.
[8] B. Demir, K. Chan, D. J. Searles, *Macromolecules* **2020**, *53*, 7635.
[9] Y. Fu, Y. Chen, H. Zhou, Y. Li, *Composites, Part A* **2025**, *188*, 108589.

© 2025 The Author(s). Advanced Energy and Sustainability Research published by Wiley-VCH GmbH

26999412, 0, Downloaded from https://advanced.onlinelibrary.wiley.com/doi/10.1002/aesr.202500222 by Universidade do Porto, Wiley Online Library on [21/10/2025]. See the Terms and Conditions (https://onlinelibrary.wiley.com/terms-and-conditions) on Wiley Online Library for rules of use; OA articles are governed by the applicable Creative Commons License

[10] N. S. Grundish, J. B. Goodenough, H. Khani, *Curr. Opin. Electrochem.* **2021**, *30*, 100828.
[11] X. Yu, A. Manthiram, *Energy Storage Mater.* **2021**, *34*, 282.
[12] G. Yu, L. Pan, H. Zhang, Y. Wang, K. Li, D. Chen, J. Chen, Z. M. Sun, *Adv. Energy Sustainability Res.* **2022**, *3*, 2100193.
[13] Y. Fu, Z. Gu, Q. Gan, Y.-W. Mai, *Mater. Sci. Eng., R* **2024**, *160*, 100815.
[14] M. Niazi, F. Danzi, P. P. Camanho, *J. Appl. Polym. Sci.* **2025**, e57945, https://doi.org/10.1002/app.57945.
[15] R. Liu, M. Liu, S. Wu, X. Che, J. Dong, J. Yang, *Eur. Polym. J.* **2020**, *137*, 109948.
[16] Y. Zhou, J. Pan, X. Ou, Q. Liu, Y. Hu, W. Li, R. Wu, J. Wen, F. Yan, *Adv. Energy Mater.* **2021**, *11*, 2102047.
[17] L. Herbers, J. Minář, S. Stuckenberg, V. Küpers, D. Berghus, S. Nowak, M. Winter, P. Bieker, *Adv. Energy Sustainability Res.* **2023**, *4*, 2300153.
[18] S.-H. Wang, P.-L. Kuo, C.-T. Hsieh, H. Teng, *ACS Appl. Mater. Interfaces* **2014**, *6*, 19360.
[19] Q. Zhou, X. Yang, X. Xiong, Q. Zhang, B. Peng, Y. Chen, Z. Wang, L. Fu, Y. Wu, *Adv. Energy Mater.* **2022**, *12*, 2201991.
[20] H. Luo, S. Ma, J. Liu, Y. Luo, X. Gao, *Eur. Polym. J.* **2023**, *194*, 112184.
[21] D. Xu, J. Jin, C. Chen, Z. Wen, *ACS Appl. Mater. Interfaces* **2018**, *10*, 38526.
[22] B. Hou, X. Li, M. Yan, Q. Wang, *Eur. Polym. J.* **2023**, *185*, 111826.
[23] D. M. Reinoso, M. A. Frechero, *Energy Storage Mater.* **2022**, *52*, 430.
[24] C. M. Costa, E. Lizundia, S. Lanceros-Méndez, *Prog. Energy Combust. Sci.* **2020**, *79*, 100846.
[25] W. Yao, Q. Zhang, F. Qi, J. Zhang, K. Liu, J. Li, W. Chen, Y. Du, Y. Jin, Y. Liang, N. Liu, *Electrochim. Acta* **2019**, *318*, 302.
[26] M. A. Raja, S. H. Lim, D. Jeon, S. Bae, W. Oh, I. Yang, D. Kang, J. Ha, H. E. Lee, I.-K. Oh, S. Kim, S. Kim, *ACS Appl. Mater. Interfaces* **2024**, *16*, 59128.
[27] A. Manfo, S. Konwar, P. K. Singh, R. M. Mehra, Y. Kumar, M. Gupta, *Mater. Today: Proc.* **2021**, *34*, 802.
[28] B. Ravikumar, M. Mynam, B. Rai, *J. Phys. Chem. C* **2018**, *122*, 8173.
[29] N. Ataollahi, A. Ahmad, H. Hamzah, M. Y. A. Rahman, N. S. Mohamed, *Int. J. Electrochem. Sci.* **2012**, *7*, 6693.
[30] Z. Li, J. Fu, X. Zhou, S. Gui, L. Wei, H. Yang, H. Li, X. Guo, *Adv. Sci.* **2023**, *10*, 2201718.
[31] L. Hu, X. Gao, H. Wang, Y. Song, Y. Zhu, Z. Tao, B. Yuan, R. Hu, *Small* **2024**, *20*, 2312251.
[32] W. Qin, Q. Yang, Y. He, L. Zhang, H. Hu, *Mech. Mater.* **2023**, *185*, 104773.
[33] Z. Shen, Y. Cheng, S. Sun, X. Ke, L. Liu, Z. Shi, *Carbon Energy* **2021**, *3*, 482.
[34] H. Liu, C. Liu, Y. Zhou, Y. Zhang, W. Deng, G. Zou, H. Hou, X. Ji, *Energy Storage Mater.* **2024**, 103575.
[35] N. Ding, S. W. Chien, T. L. D. Tam, X. Li, G. Wu, W. J. Lee, S. Y. Chiam, Y. S. Meng, D. W. H. Fam, *Adv. Energy Mater.* **2024**, *14*, 2402986.
[36] H. Chen, D. Adekoya, L. Hencz, J. Ma, S. Chen, C. Yan, H. Zhao, G. Cui, S. Zhang, *Adv. Energy Mater.* **2020**, *10*, 2000049.
[37] T. Jiang, P. He, G. Wang, Y. Shen, C.-W. Nan, L.-Z. Fan, *Adv. Energy Mater.* **2020**, *10*, 1903376.
[38] G.-R. Zhu, Q. Zhang, Q.-S. Liu, Q.-Y. Bai, Y.-Z. Quan, Y. Gao, G. Wu, Y.-Z. Wang, *Nat. Commun.* **2023**, *14*, 4617.
[39] K. M. Kim, N.-G. Park, K. S. Ryu, S. H. Chang, *Electrochim. Acta* **2006**, *51*, 5636.
[40] K. Hong, J. Yuk, H. J. Kim, J. Y. Lee, S. Kim, J.-L. Lee, K. H. Lee, *Composites, Part B* **2018**, *152*, 275.
[41] H. Peng, T. Long, J. Peng, H. Chen, L. Ji, H. Sun, L. Huang, S.-G. Sun, *Adv. Energy Mater.* **2024**, *14*, 2400428.
[42] C. M. Branco, S. Sharma, M. M. C. Forte, R. Steinberger-Wilckens, *J. Power Sources* **2016**, *316*, 139.
[43] V. Vijayakumar, B. Anothumakkool, S. Kurungot, M. Winter, J. Ravi Nair, *Energy Environ. Sci.* **2021**, *14*, 2708.
[44] G. Foran, D. Mankovsky, N. Verdier, D. Lepage, A. Prébé, D. Aymé-Perrot, M. Dollé, *iScience* **2020**, *23*, 101597.
[45] E. F. Hansen, *MRS Online Proc. Libr.* **1995**, *352*, 807.
[46] S. Pandey, S. K. Pandey, V. Parashar, G. K. Mehrotra, A. C. Pandey, *J. Mater. Chem.* **2011**, *21*, 17154.
[47] G. Ek, F. Jeschull, T. Bowden, D. Brandell, *Electrochim. Acta* **2017**, *246*, 208.
[48] H. Yang, N. Wu, *Energy Sci. Eng.* **2022**, *10*, 1643.
[49] C.-C. Yang, *Mater. Lett.* **2004**, *58*, 33.
[50] HB QUIMICA, LDA. Ficha Técnica: HB AS 89/AW 89. https://www.hbquimica.pt, **2011**. Revisão nr. 01, Código Tradução C009-T, (accessed: 2024).
[51] S. El-Sayed, K. H. Mahmoud, A. A. Fatah, A. D. S. C. Hassen, *Phys. B* **2011**, *406*, 4068.
[52] A. Alakanandana, A. R. Subrahmanyam, J. Siva Kumar, *Mater. Today: Proc.* **2016**, *3*, 3680.
[53] D. M. T. Mustafa, S. Rostam, S. B. Aziz, *Adv. Mater. Sci. Eng.* **2020**, *2020*, 7914796.
[54] R. Muchakayala, S. Song, S. Gao, X. Wang, Y. Fan, *Polym. Test.* **2017**, *58*, 116.
[55] J. Tang, R. Muchakayala, S. Song, M. Wang, K. Naveen Kumar, *Polym. Test.* **2016**, *50*, 247.
[56] S. Deng, M. Hou, L. Ye, *Polym. Test.* **2007**, *26*, 803.
[57] U. Zaheer, A. A. Khurram, T. Subhani, *Adv. Compos. Hybrid Mater.* **2018**, *1*, 705.
[58] W. K. Patrick Lim, M. Mariatti, W. S. Chow, K. T. Mar, *J. Fire Sci.* **2012**, *30*, 428.
[59] K. Laoubi, Z. Hamadi, A. Ahmed Benyahia, A. Serier, Z. Azari, *Composites, Part B* **2014**, *56*, 520.
[60] P. Vadhva, J. Hu, M. J. Johnson, R. Stocker, M. Braglia, D. J. L. Brett, A. J. E. Rettie, *ChemElectroChem* **2021**, *8*, 1930.
[61] J. Xiao, Q. Li, Y. Bi, M. Cai, B. Dunn, T. Glossmann, J. Liu, T. Osaka, R. Sugiura, B. Wu, J. Yang, J. G. Zhang, M. S. Whittingham, *Nat. Energy* **2020**, *5*, 561.
[62] Y. Yao, J. Lei, Y. Shi, F. Ai, Y.-C. Lu, *Nat. Energy* **2021**, *6*, 582.
[63] Y. Lin, M. Wu, J. Sun, L. Zhang, Q. Jian, T. Zhao, *Adv. Energy Mater.* **2021**, *11*, 2101612.
[64] F. Xu, Y. Wu, L. Wang, Z. Zhang, G. Liu, C. Guo, D. Wu, C. Yi, J. Luo, W. He, C. Xu, M. Yang, H. Li, L. Chen, F. Wu, C. Xu, M. Yang, H. Li, L. Chen, F. Wu, *Adv. Energy Mater.* **2025**, *11*, 2101612.
[65] R. Wang, C. Tian, X. Li, T. Li, Y. Fang, K. Pan, Z. Zhou, *Adv. Funct. Mater.* **2025**, *35*, e16074.
[66] Z. Zhang, Y. Huang, H. Gao, C. Li, J. Huang, P. Liu, *J. Membr. Sci.* **2021**, *621*, 118940.
[67] G.-H. Dong, Y.-Q. Mao, G.-M. Yang, Y.-Q. Li, S.-F. Song, C.-H. Xu, P. Huang, N. Hu, S.-Y. Fu, *ACS Appl. Energy Mater.* **2021**, *4*, 4038.
[68] J. Lee, B.-N. Park, *J. Phys. Chem. Lett.* **2024**, *15*, 7095.

© 2025 The Author(s). Advanced Energy and Sustainability Research published by Wiley-VCH GmbH

26999412, 0, Downloaded from https://advanced.onlinelibrary.wiley.com/doi/10.1002/aesr.202500222 by Universidade do Porto, Wiley Online Library on [21/10/2025]. See the Terms and Conditions (https://onlinelibrary.wiley.com/terms-and-conditions) on Wiley Online Library for rules of use; OA articles are governed by the applicable Creative Commons License